

Evidence for two-gap superconductivity in the non-centrosymmetric compound LaNiC_2

J. Chen,¹ J. L. Zhang,^{1,2} L. Jiao,¹ Y. Chen,¹ L. Yang,¹ M. Nicklas,² F. Steglich,² and H. Q. Yuan^{1,*}

¹*Department of Physics and Center for Correlated Matter,
Zhejiang University, Hangzhou, Zhejiang 310027, China*

²*Max Planck Institute for Chemical Physics of Solids, D-01187 Dresden, Germany*

(Dated: May 25, 2022)

We study the superconducting properties of the non-centrosymmetric compound LaNiC_2 by measuring the London penetration depth $\Delta\lambda(T)$, the specific heat $C(T, B)$ and the electrical resistivity $\rho(T, B)$. Both $\Delta\lambda(T)$ and the electronic specific heat $C_e(T)$ exhibit exponential behavior at low temperatures and can be described in terms of a phenomenological two-gap BCS model. The residual Sommerfeld coefficient in the superconducting state, $\gamma_0(B)$, shows a fast increase at low fields and then an eventual saturation with increasing magnetic field. A pronounced upturn curvature is observed in the upper critical field $B_{c2}(T)$ near T_c . All the experimental observations support the existence of two-gap superconductivity in LaNiC_2 .

PACS numbers: 74.70.Wz; 74.20.Rp; 74.25.Op

I. INTRODUCTION

The spatial-inversion and time-reversal symmetries of a superconductor (SC) may impose important constraints on the pairing states. Among the SCs discovered in the past, most of them possess a center of inversion symmetry. In this case, the Cooper pairs are either in an even-parity spin-singlet or odd-parity spin-triplet pairing state, constrained by the Pauli principle and parity conservation.^{1,2} However, the tie between spatial symmetry and the Cooper-pair spins is violated in SCs lacking spatial inversion symmetry.³⁻⁷ In the non-centrosymmetric (NCS) SCs, an asymmetric electrical field gradient may yield an antisymmetric spin-orbit coupling (ASOC), which splits the Fermi surface into two subsurfaces of different spin helicities, with pairing allowed both across each one of the subsurfaces and between the two. The parity operator is then no longer a well-defined symmetry of the crystal, and allows the admixture of spin-singlet and spin-triplet pairing states within the same orbital channel.

NCS superconductivity has been intensively studied in a few heavy fermion compounds, e.g., CePt_3Si ,⁸⁻¹¹ CeRhSi_3 ,¹² CeIrSi_3 ¹³ and UIr .¹⁴ In these systems, the nature of superconductivity is complicated by its coexistence with magnetism and the lack of inversion symmetry; both effects may give rise to unconventional superconductivity. It is, therefore, highly desired to search for weakly correlated, non-magnetic NCS SCs to study the pure effect of ASOC on superconductivity. It has been demonstrated that, in $\text{Li}_2(\text{Pd}_{1-x}\text{Pt}_x)_3\text{B}$, the spin-singlet and spin-triplet order parameters can add constructively and destructively¹⁵. The mixing ratio in this compound appears to be tunable by the strength of ASOC;¹⁵ $\text{Li}_2\text{Pd}_3\text{B}$ behaves like a BCS SC, but $\text{Li}_2\text{Pt}_3\text{B}$ shows evidence of spin-triplet pairing state¹⁵⁻¹⁷ attributed to an enhanced ASOC.¹⁸ Recently, non-BCS-like superconductivity with a possible nodal gap structure at low temperatures was observed in Y_2C_3 ¹⁹, in spite of its relatively weak ASOC. On the other hand, evidence of multi-gap superconductivity was shown in La_2C_3 ²⁰ and $\text{Mg}_{10}\text{Ir}_{19}\text{B}_{16}$.²¹ The diversity of the superconducting states in the NCS SCs requires more systematic investigations in order to reach a unified picture.

LaNiC_2 , a simple metallic NCS SC,²² has recently drawn considerable attention. However, the order parameter of this compound remains highly controversial. Measurements of specific heat²³ and $\text{NQR-}1/T_1$ ²⁴ suggested that LaNiC_2 is a conventional BCS SC which is further supported by theoretical calculations.²⁵ On the other hand, evidence of possible nodal superconductivity was inferred from the recent penetration depth which follows $\Delta\lambda(T) \sim T^n$ ($n \geq 2$)²⁶ and also from the early measurements of specific heat by W. H. Lee, et al.²⁷ Unconventional characteristics were also revealed from μSR experiments in which the absence of time-reversal symmetry was indicated.^{28,29} In order to elucidate the pairing state of LaNiC_2 here, we present a systematic study of the penetration depth $\Delta\lambda(T)$, the electronic specific heat $C_e(T, B)$ and the electrical resistivity $\rho(T, B)$ on high quality polycrystalline samples. We found that the temperature dependence of both $\Delta\lambda(T)$ and $C_e(T)$ can be well described by a phenomenological two-gap BCS model. The residual Sommerfeld coefficient, $\gamma_0(B)$, increases fast at low fields and eventually saturates with increasing magnetic field. Furthermore, the upper critical field $B_{c2}(T)$ shows an upward curvature near T_c . All these observations resemble those of MgB_2 ,³⁰⁻³³ strongly supporting a two-gap SC in LaNiC_2 .

II. EXPERIMENTAL METHODS

Polycrystalline LaNiC_2 was synthesized by arc melting. A Ti button was used as an oxygen getter. Appropriate amounts of the constituent elements (3N-purity La, 2N-purity Ni and 3N-purity graphite) were pressed into a disk before arc-melting. The ingot was inverted and remelted for several times to ensure sample homogeneity. The derived ingot, with a negligible weight loss, was annealed at 1050°C in a vacuum-sealed quartz tube for 7 days, and then quenched into water at room temperature.

A small portion of the ingot was ground into fine powders for X-ray diffraction (XRD) measurements on a X'Pert PRO diffractometer (Cu K radiation) in the Bragg-Brentano geometry. Measurements of the electrical resistivity, specific heat and magnetization were performed in a 9T-PPMS and a

5T-MPMS (Quantum Design), respectively. Precise measurements of the London penetration depth $\Delta\lambda(T)$ were performed utilizing a tunnel diode oscillator (TDO) technique³⁴ at a frequency of 7MHz down to 0.37K in a ³He cryostat.

III. RESULTS AND DISCUSSION

A. Sample characterizations

Fig.1 shows the XRD patterns of LaNiC₂ which identify it as a single phase. The Rietveld refinement confirmed an orthorhombic Amm2 structure (No. 38). The atoms of Ni (2b) and C (4e) are alternatively stacked on the NiC₂ plane but lose the inversion symmetry, as shown in the inset of Fig.1. The derived lattice parameters are given as $a=3.9599\text{\AA}$, $b=4.5636\text{\AA}$ and $c=6.2031\text{\AA}$, in good agreement with those reported in literature.²²

Fig.2(a) presents the temperature dependence of the electrical resistivity $\rho(T)$ between 2K and 300K at $B=0$, which shows simple metallic behavior above T_c . Observations of a large residual resistivity ratio ($\text{RRR}=\rho_{300\text{K}}/\rho_{4\text{K}}\approx 26$) and a sharp superconducting transition ($T_c^p\approx 3.5\text{K}$) suggest a high quality of our samples. Fig.2(b) shows the temperature dependence of the specific heat $C(T)/T$ at $B=0$ and the zero-field-cooling (ZFC) magnetization $M(T)$ ($B=10\text{ Oe}$), respectively. A pronounced superconducting transition seen in both $C(T)/T$ and $M(T)$ confirms the bulk superconductivity in LaNiC₂. The bulk T_c , derived from the specific heat ($T_c^{C_p}=2.75\text{K}$) and the magnetization ($T_c^M=3.1\text{K}$), are slightly lower than the resistive T_c^p , which is likely due to the residual sample inhomogeneity. It is noted that the magnetization $M(T)$ exhibits temperature-independent Pauli-paramagnetic behavior above T_c , ruling out any visible magnetic impurity in our samples. Furthermore, the above physical quantities were measured on different samples cut from the same batch; the con-

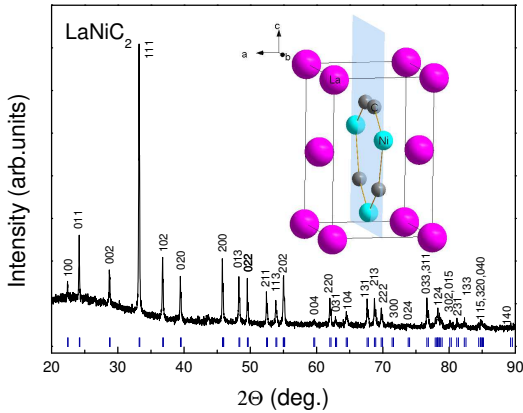


FIG. 1: (Color online) The XRD patterns and crystal structure of LaNiC₂. Short vertical bars indicate the calculated reflection positions.

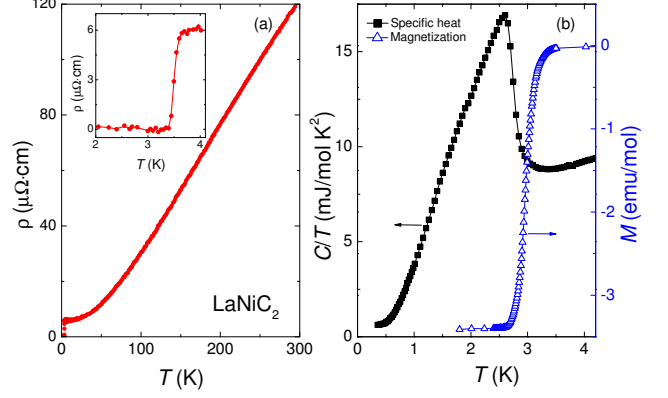


FIG. 2: (Color online) Temperature dependence of the electrical resistivity $\rho(T)$ (a), specific heat $C(T)/T$ (b, left axis) and dc magnetization $M(T)$ (b, right axis) for LaNiC₂. The electrical resistivity and specific heat are measured at zero field, and the magnetization is measured at 100e (ZFC).

sistent experimental results and fitting parameters, as shown below, again indicate a good sample quality. Based on the RRR value and the width of the superconducting transition, our samples have a quality better or compatible with the best samples reported in literature.^{26,27} The small value of $\gamma_n=7.7\text{mJ/molK}^2$ above T_c indicates the absence of strong electronic correlations in LaNiC₂.

B. London penetration depth

The London penetration depth is an important superconducting parameter. The TDO-based technique can accurately measure the temperature dependence of the resonant frequency shift $\Delta f(T)$, which is proportional to the changes of the penetration depth, i.e., $\Delta\lambda(T)=G\cdot\Delta f(T)$. Here the G factor is a constant which is solely determined by the sample and coil geometries.³⁴ Fig.3(a) presents the temperature dependence of the penetration depth $\Delta\lambda(T)$ for LaNiC₂, where $G=11\text{\AA/Hz}$. In the left inset, $\Delta\lambda(T)$ is plotted over the full temperature range of our measurement from which a sharp superconducting transition can be seen. In the main figure of Fig.3(a), we show $\Delta\lambda(T)$ at low temperatures, along with the fittings of a quadratic temperature dependence (dashed line), a conventional BCS model (dotted line) and a two-gap BCS model (solid line). For an isotropic one-gap BCS model, the penetration depth at $T\ll T_c$ is given by:

$$\Delta\lambda(T) \approx \lambda_0 \sqrt{\frac{\pi\Delta_0}{2T}} e^{-\frac{\Delta_0}{T}}, \quad (1)$$

where Δ_0 is the energy gap at $T=0$; $\Delta_0=1.76T_c$ for the conventional BCS SCs.

One can see from Fig.3(a) that the penetration depth at low temperatures is not well described in terms of either the

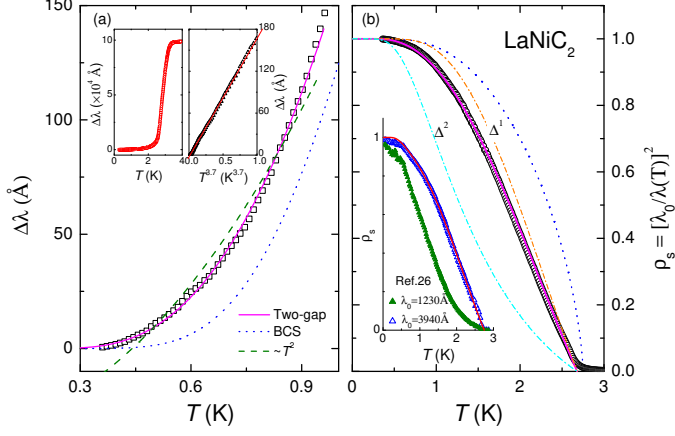


FIG. 3: (Color online) (a) Temperature dependence of the penetration depth $\Delta\lambda(T)$ at low temperatures for LaNiC_2 . The left inset shows $\Delta\lambda(T)$ in the full temperature range of our measurement. The right inset shows $\Delta\lambda(T)$ vs. $T^{3.7}$ in the temperature range of $0.35\text{K} \leq T \leq 1\text{K}$. (b) Temperature dependence of the superfluid density $\rho_s(T) = [\lambda_0/\lambda(T)]^2$. The inset shows $\rho_s(T)$ from Ref.26 with $\lambda_0 = 1230\text{\AA}$ and 3940\AA , together with a fit of a two-gap BCS model (solid line). In the main plots, the solid and dotted lines represent fittings of a two-gap and conventional BCS model, respectively. The dashed line in (a) shows a fit of $\Delta\lambda(T) \sim T^2$ to the experimental data. The dashed-dotted lines in (b) present the respective contributions to $\rho_s(T)$ from the two superconducting gaps of Δ^1 and Δ^2 .

conventional BCS model or the quadratic temperature dependence; the latter is expected for superconductors with point nodes. Instead, it can be fitted equally well by a power-law dependence of $\Delta\lambda(T) \propto T^{3.7}$ (right inset of Fig.3(a)), or by a two-gap BCS model. Practically, the penetration depth of a two-gap SC can be fitted by a power-law temperature dependence with a large exponent of $n > 3$, whose value may depend on the fitting temperature region. In the following, we will analyze the penetration depth and its corresponding superfluid density, $\rho_s(T)$, in terms of the phenomenological two-gap BCS model, which is further supported by the specific heat and the upper critical field (see below).

According to the phenomenological two-gap BCS model, which has been successfully applied to MgB_2 ,³⁰ the superfluid density $\rho_s(T)$ can be expressed as:

$$\rho_s(T) = x\rho_s(\Delta^1, T) + (1-x)\rho_s(\Delta^2, T), \quad (2)$$

where x is the relative weight for Δ^1 . The normalized superfluid density for each band is given by

$$\rho_s(\Delta, T) = 1 - \frac{2}{T} \int_0^\infty f(\epsilon, T) \cdot [1 - f(\epsilon, T)] d\epsilon, \quad (3)$$

where $f(\epsilon, T) = (1 + e^{\sqrt{\epsilon^2 + \Delta^2(T)}/T})^{-1}$ is the Fermi distribution function. Here we adopt the following temperature dependence of the gap function:³⁵

$$\Delta(T) = \Delta_0 \tanh\left[\frac{\pi T_c}{\Delta_0} \sqrt{a \frac{\Delta C}{C} \left(\frac{T_c}{T} - 1\right)}\right], \quad (4)$$

where $\frac{\Delta C}{C}$ denotes the specific heat jump at T_c and $a = 2/3$.

In Fig.3(b), we plot the superfluid density $\rho_s(T)$ converted from the penetration depth by $\rho_s(T) = [\lambda_0/\lambda(T)]^2$, where $\lambda(T) = \lambda_0 + \Delta\lambda(T)$. The zero-temperature penetration depth, $\lambda_0 \approx 3940\text{\AA}$, is estimated from $\lambda_0 = \frac{1}{\Delta_0 T_c} \sqrt{\frac{\Phi_0 B_{c2}(0)}{24\gamma_n}}$, as derived from both the BCS and Ginzburg-Landau theories for a type-II SC.³⁵ Here we take the experimental values of $T_c = 2.75\text{K}$, $B_{c2}^C(0) \approx 0.48\text{T}$ and $\gamma_n = 7.7\text{mJ/molK}^2$ from the specific heat (see below), and Φ_0 is the flux quantum. Indeed, both the penetration depth $\Delta\lambda(T)$ and the superfluid density $\rho_s(T)$ can be well described by the two-gap BCS model (solid lines), from which we obtained the gap parameters of $\Delta_0^1 = 2.0T_c$, $\Delta_0^2 = 1.0T_c$ and $x = 0.8$. $T_c = 2.7\text{K}$ is obtained from the best fit of the superfluid density which is consistent with the penetration depth drop. The individual contribution to the total superfluid density $\rho_s(T)$ from the respective order parameters Δ^1 and Δ^2 is shown in Fig.3(b), from which one can see that the large gap has a dominant contribution. For comparison, we replot $\rho_s(T)$ from Ref.26 in the inset of Fig.3(b) which are converted from the penetration depth data by using $\lambda_0 = 1230\text{\AA}$ (from Ref.26) and 3940\AA (in this study). The superfluid density $\rho_s(T)$ from Ref.26 is in reasonable agreement with our results if $\lambda_0 = 3940\text{\AA}$ is used. Furthermore, one can also fit its superfluid density $\rho_s(T)$ by the two-gap BCS model at temperature above 0.5K . The derived parameters of $\Delta_0^1 = 1.9T_c$, $\Delta_0^2 = 0.7T_c$ and $x = 0.75$ are consistent with our results. As a first approximation, two-gap-like superconductivity is expected in NCS SCs with a moderate ASOC strength, in which the spin degenerate bands are split by the ASOC, but the triplet component is not yet dominant. Nevertheless, it is still possible that a weak linear term of $\Delta\lambda(T)$ may develop at very low temperatures as seen in Y_2C_3 .¹⁹ At present, we cannot exclude such a possibility in LaNiC_2 as argued in Ref.26. More precise measurements of the penetration depth at lower temperatures are desired to resolve this issue.

C. Specific heat

In the upper inset of Fig.4, we plot the total specific heat $C(T)$ as a function of temperature for LaNiC_2 , which was obtained after subtracting the addenda contributions from the raw data. At temperatures above T_c ($3.5\text{K} \leq T \leq 20\text{K}$), $C(T)$ follows a polynomial expansion of $C(T) = \gamma_n T + B_3 T^3 + B_5 T^5 + B_7 T^7$, in which $C_e = \gamma_n T$ and $C_{ph} = B_3 T^3 + B_5 T^5 + B_7 T^7$ represent the electronic and phonon contributions, respectively. This yields the Sommerfeld coefficient in the normal state, $\gamma_n = 7.7\text{mJ/molK}^2$, and the Debye temperature $\Theta_D = 450\text{K}$, the latter being derived from $B_3 = N\pi^4 R \Theta_D^{-3} 12/5$, where $R = 8.314\text{J/molK}$, $N = 4$ and $B_3 = 0.085\text{mJ/molK}^4$. The specific heat jump at T_c , i.e., $\Delta C/\gamma_n T_c = 1.05$, is lower than the BCS value of 1.43, which might arise from the multi-gap structure as seen in MgB_2 or the gap anisotropy.³²

In the superconducting state, the total heat capacity C is the sum of a B -dependent electronic contribution C_e , a B -independent lattice contribution C_{ph} and a small B -dependent Schottky contribution C_{Sch} . We obtained the electronic spe-

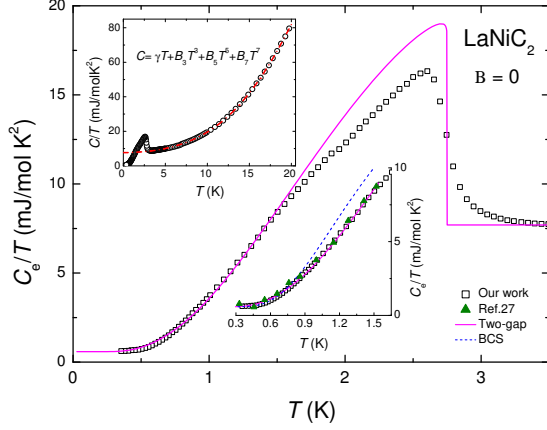


FIG. 4: (Color online) Temperature dependence of the specific heat at zero field for LaNiC₂. The upper inset shows the total specific heat $C(T)/T$ and its polynomial fitting of $C(T) = \gamma_n T + B_1 T^3 + B_3 T^5 + B_7 T^7$. The main figure plots the electronic specific heat $C_e(T)/T$ after subtracting the phonon contributions. The solid and dashed lines present fittings of a two-gap and conventional BCS model, respectively. The lower inset expands the low- T section of our work and also the data from Ref.27.

sific heat C_e by subtracting the B -independent phonon contribution C_{ph} and B -dependent C_{Sch} using the following two methods. The first one is to directly subtract the phonon contribution of C_{ph} from the total heat capacity by

$$C_e(B, T) = C(B, T) - C_{ph}(T). \quad (5)$$

In the second method, we calculate the electronic specific heat C_e in the superconducting state by using the reference value at $B = 1\text{ T}$ where superconductivity is suppressed, i.e.,³²

$$C_e(B, T) = C(B, T) - C(1\text{ T}, T) + \gamma_n(1\text{ T}) \cdot T. \quad (6)$$

Indeed, both methods give nearly identical results of C_e at $T < T_c$, indicating that the B -dependent C_{Sch} is negligible in the temperature and magnetic field ranges of our measurements. In the following, we will present the electronic specific heat $C_e(T)$ derived from Eq.(5).

In Fig.4, we plot the electronic specific heat $C_e(T)/T$ of LaNiC₂ at zero field, which shows an exponential-type behavior at low temperatures, together with the fittings of conventional and two-gap BCS models. For a system of independent fermion quasiparticles, the entropy, S , can be calculated by³¹

$$\frac{S(\Delta, T)}{\gamma_n T_c} = -\frac{6}{\pi^2} \frac{\Delta(T)}{T_c} \int_0^\infty f(\epsilon, T) \cdot \ln f(\epsilon, T) + [1 - f(\epsilon, T)] \cdot \ln[1 - f(\epsilon, T)] d\epsilon. \quad (7)$$

For a two-gap BCS SC, the entropy expression can be generalized as follows:³¹

$$S(T) = xS(\Delta^1, T) + (1-x)S(\Delta^2, T). \quad (8)$$

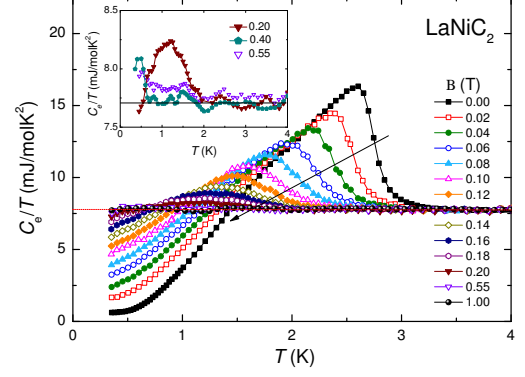


FIG. 5: (Color online) Temperature dependence of the electronic specific heat $C_e(T)/T$ at various magnetic fields for LaNiC₂. The dashed horizontal line represents γ_n . The magnetic field increases along the arrow direction. The inset shows the electronic specific heat $C_e(T)/T$ at magnetic fields near $B_{c2}(0)$.

Differentiation of Eq.(8) gives the total electronic specific heat C_e in the superconducting state by $C_e(T) = TdS(T)/dT$. The specific heat data of LaNiC₂ is fitted over a temperature range of 0.35-1.5K. The two-gap BCS model (solid line) fits much better than the conventional BCS model (dashed line), as clearly seen in the lower inset of Fig.4. The former fitting gives the parameters of $\Delta_0^1 = 2.3T_c$, $\Delta_0^2 = 1.25T_c$ and $x=0.75$ for Δ_0^1 , which are close to those obtained from the superfluid density $\rho_s(T)$. For comparison, we also plot the specific heat data derived in Ref.27 with our results in the lower inset of Fig.4. Remarkably, these two sets of data are exactly the same. It is noted that the original fits of $C_e \sim T^3$ from Ref.27 was at relatively high temperatures, and a deviation exists in the low temperature limit. For a two-gap SC, the interband coupling ensures that the two gaps open at the same T_c . Usually, the main contributions to both the electronic specific heat C_e and the superfluid density ρ_s stem from the larger gap Δ^1 at temperatures just below T_c , but the physical behavior can be modified at lower temperatures attributed to the opening of a smaller gap Δ^2 .

In Fig.5, the temperature dependence of the electronic specific heat $C_e(T)/T$ is shown at various magnetic fields for LaNiC₂. Obviously, the superconducting transition is shifted to lower temperatures, and becomes broadened with increasing magnetic field, resembling that of the two-gap SC, MgB₂.³² The inset in Fig.5 describes the specific heat near the upper critical field in detail. One can see that the superconducting transition still exists at $B = 0.40\text{ T}$ but vanishes at $B = 0.55\text{ T}$. This suggests a bulk upper critical field of $B_{c2}^p(0) < 0.55\text{ T}$, which is much lower than the resistive upper critical field ($B_{c2}^r(0) \approx 1.67\text{ T}$, see below). The underlying reason for such a discrepancy remains unclear. Similar observations were also made for other unconventional SCs. For instance, the heavy fermion CeIrIn₅ shows a much larger resistive T_c ($\approx 1.3\text{ K}$) than the bulk T_c ($\approx 0.4\text{ K}$), resulting in a large differ-

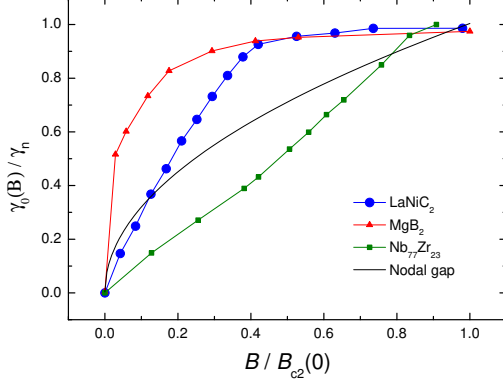


FIG. 6: (Color online) Magnetic field dependence of the residual Sommerfeld coefficient plotted as $\gamma_0(B)/\gamma_n$ vs. $B/B_{c2}(0)$ for LaNiC_2 (this work), MgB_2 ³² and $\text{Nb}_{77}\text{Zr}_{23}$ ³⁷. The solid line shows the case of nodal superconductivity, i.e., $\gamma_0(B) \propto B^{1/2}$.

ence in the corresponding upper critical fields.³⁶

The residual Sommerfeld coefficient in the superconducting state, $\gamma_0(B)$, which describes the low-energy quasiparticle excitations, provides important insights into the superconducting pairing symmetry. In fully gapped BCS SCs, the low-lying excitations are usually confined to the vortex cores and the specific heat is, therefore, proportional to the vortex density which increases linearly with increasing magnetic field, i.e., $\gamma_0(B) \propto B$.³⁸ On the other hand, for a highly anisotropic or gapless SC, the quasiparticle excitations can spread outside the vortex cores which can, in fact, significantly contribute to the specific heat at low temperatures. The local supercurrent flow may give rise to a shift on the excitation energy (Doppler shift), resulting in a distinct magnetic field dependence of the density of state, $N(E_F)$, at the Fermi energy. In SCs with line nodes, Volovik showed that $N(E_F) \propto B^{1/2}$, leading to a square-root field dependence of the residual Sommerfeld coefficient, i.e., $\gamma_0(B) \propto B^{1/2}$.³⁹ In Fig.6, we present the normalized Sommerfeld coefficient, $\gamma_0(B)/\gamma_n$, as a function of $B/B_{c2}(0)$ for LaNiC_2 . Here the values of $\gamma_0(B)$ are determined at $T=0.35\text{K}$ after subtracting the small non-zero fraction at zero magnetic field. One can see that $\gamma_0(B)$ of LaNiC_2 shows a fast increase at low fields and then saturates with increasing magnetic field, clearly deviating from the linear field dependence expected for a conventional BCS SC like $\text{Nb}_{77}\text{Zr}_{23}$ (squares),³⁷ and also from the square-root field dependence expected for a nodal SC (solid line). The curvature of $\gamma_0(B)$ is rather similar to that of the prototypical two-gap SC, MgB_2 ,³² and also the residual thermal conductivity κ_0/T of the multiband SC, $\text{PrRu}_4\text{Sb}_{12}$,⁴⁰ providing another unambiguous evidence of two-gap superconductivity for LaNiC_2 .

D. Electrical resistivity and upper critical field

Fig.7 shows the temperature dependence of the electrical resistivity $\rho(T)$ at various magnetic fields ($B=0-1.5\text{T}$) for

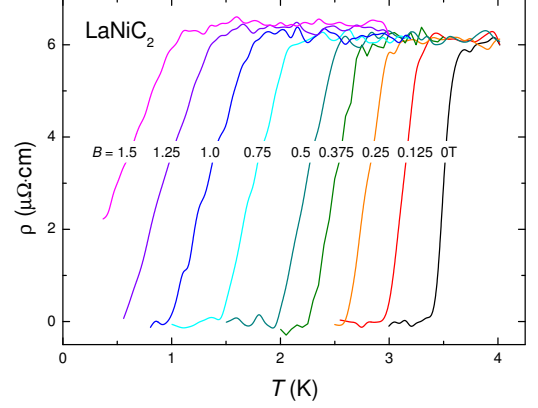


FIG. 7: (Color online) Temperature dependence of the electrical resistivity $\rho(T)$ at various magnetic fields for LaNiC_2 .

LaNiC_2 . The superconducting transition is eventually suppressed, and the transition width is slightly broadened upon applying a magnetic field. The temperature dependence of the upper critical field $B_{c2}(T)$ is plotted in the inset of Fig.8, in which T_c is determined from the mid-point of the superconducting transition and the error bars are defined by 10% and 90% of the normal-state resistivity just above T_c .

For comparison, in Fig.8 we show the normalized upper critical field, $B_{c2}/[T_c(dB_{c2}/dT)_{T_c}]$, vs. T/T_c for several representative SCs, i.e., LaNiC_2 (this study), MgB_2 ³³ and $\text{Li}_2\text{Pt}_3\text{B}$.⁴¹ One can see that the upper critical fields $B_{c2}(T)$ of LaNiC_2 , derived from both the specific heat (stars) and the resistivity (squares), follow the same scaling behavior even though the corresponding T_c is different. We fit the $B_{c2}(T)$ data of LaNiC_2 with the Werthamer-Helfand-Hohenberg (WHH) theory in the dirty limit.⁴² A clear deviation is observed at low temperatures, and the experimental value of $B_{c2}(0)$ exceeds that of the WHH predictions. A positive curvature of $B_{c2}(T)$ near T_c and the enhancement of $B_{c2}(0)$ are typical features of multi-gap SCs, arising from the contributions of the small gap at low temperatures. Indeed, the upper critical field $B_{c2}(T)$ of LaNiC_2 remarkably resembles that of MgB_2 ,³³ as seen in Fig.8.

To further characterize $B_{c2}(T)$, we analyze it in terms of a two-gap BCS model. In the dirty limit, the upper critical field $B_{c2}(T_c)$ takes the following form:⁴³

$$a_0[\ln t + U(h)][\ln t + U(\eta h)] + a_1[\ln t + U(h)] + a_2[\ln t + U(\eta h)] = 0, \quad (9)$$

where $U(x) = \psi(1/2+x) - \psi(x)$, and $\psi(x)$ is the di-gamma function. The asymptotic value of $B_{c2}(0)$ can be obtained by the following quadratic equation:

$$B_{c2}(0) = \frac{\Phi_0 T_c}{2\gamma \sqrt{D_1 D_2}} e^{\frac{g}{2}},$$

$$g = \left(\frac{\lambda_0^2}{w^2} + \ln^2 \frac{D_2}{D_1} + \frac{2\lambda_-}{w} \ln \frac{D_2}{D_1} \right)^{1/2} - \frac{\lambda_0}{w}, \quad (10)$$

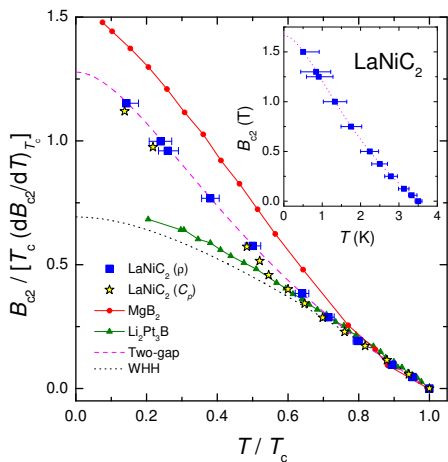


FIG. 8: (Color online) Normalized upper critical field, $B_{c2}/[T_c(dB_{c2}/dT)_{T_c}]$, versus T/T_c for LaNiC_2 (this work), MgB_2 ³³ and $\text{Li}_2\text{Pt}_3\text{B}$.⁴¹ Here the upper critical fields for LaNiC_2 are taken from the middle point of the resistive drops (\blacksquare) and the specific heat jumps (\blackstar) at T_c . The dashed and dotted lines show the fittings of a two-gap BCS model and the WHH method, respectively. Inset: the resistive upper critical field B_{c2} versus T for LaNiC_2 , fitted by a two-gap BCS model.

where $t = T/T_c$, $h = B_{c2}D_1/2\Phi_0T$, Φ_0 is the flux quantum, $\eta = D_2/D_1$, $\lambda_{\pm} = \lambda_{11} \pm \lambda_{22}$, $w = \lambda_{11}\lambda_{22} - \lambda_{12}\lambda_{21}$, $\lambda_0 = (\lambda_{\pm}^2 + 4\lambda_{12}\lambda_{21})^{1/2}$, $a_0 = 2w/\lambda_0$, $a_1 = 1 + \lambda_{-}/\lambda_0$ and $a_2 = 1 - \lambda_{-}/\lambda_0$. Here D_m represent the intraband diffusivity tensors by nonmagnetic impurities scattering, and $\lambda_{mm'}$ are the BCS superconducting coupling constants. As shown in Fig.8, the upper critical field $B_{c2}(T)$ of LaNiC_2 can be well described by the two-gap model with the coupling constants of $\lambda_{11}=0.02$, $\lambda_{22}=0.01$, $\lambda_{12}=0.001$ and $\lambda_{21}=0.1$, and the intraband diffusivity ratio of $\eta=12$. The derived upper critical field value is $B_{c2}^p(0) \approx 1.67\text{T}$ from the electrical resistivity and $B_{c2}^c(0) \approx 0.48\text{T}$ from the specific heat, respectively. In any case, the derived $B_{c2}(0)$ for LaNiC_2 is well below the Pauli paramagnetic limit of $B_{c2}^p(0) = 1.86T_c \approx 6\text{T}$, indicating an orbital pair-breaking mechanism for LaNiC_2 .

E. Discussion

As described above, two-gap BCS superconductivity in LaNiC_2 has been evidenced from the penetration depth $\Delta\lambda(T)$, the electronic specific heat $C_e(T)$, the residual Sommerfeld coefficient $\gamma_0(B)$ and the upper critical field $B_{c2}(T)$, respectively. Such a pairing state can be qualitatively interpreted in terms of the ASOC effect as argued in many NCS SCs. In LaNiC_2 , calculations of the electronic structure based on the first-principles full-potential linearized augmented plane-wave (FLAPW) method gave a band splitting of 3.1mRy ,⁴⁴ which is small in comparison with the heavy fermion NCS SCs and also $\text{Li}_2\text{Pt}_3\text{B}$ (see Table 1). In this case, the ASOC only has a moderate effect on the pairing state; both the spin-singlet and spin-triplet components may have comparable contributions to the pairing state, naturally leading to the

behavior of two-gap-like superconductivity.

Nevertheless, it seems that the diverse behavior of the NCS SCs, as summarized in Table 1, is difficult to be fully understood by a unified picture based on the ASOC effect. The heavy fermion systems typically possess a sizeable spin-orbit coupling which results in a large band splitting too. In these compounds, an extremely large upper critical field $B_{c2}(0)$, well exceeding the paramagnetic limit, and evidence of a dominant spin-triplet pairing state with line nodes in the superconducting energy gap have been observed in the Ce-based materials.^{8–10,12,13} These unconventional superconducting properties can be explained in terms of the ASOC effect, even though the strong electronic correlations and magnetism existing in these compounds may complicate the interpretation. $\text{Li}_2(\text{Pd}_{1-x}\text{Pt}_x)_3\text{B}$ provides a model system to study the ASOC effect on superconductivity in the absence of inversion symmetry.¹⁵ In $\text{Li}_2\text{Pd}_3\text{B}$, various measurements have demonstrated BCS-like superconductivity.^{15–18} With increasing Pt concentration, which corresponds to an increase of the ASOC strength, the spin-triplet component eventually grows, showing spin-triplet superconductivity in $\text{Li}_2\text{Pt}_3\text{B}$.^{15–17}

Following the extensive studies of NCS SCs in recent years, however, a growing number of compounds show properties which cannot be simply interpreted in terms of the ASOC effect. For example, the NCS SCs BaPtSi_3 ,⁵² Re_3W ⁵³ and Ir_2Ga_9 ,⁵⁴ in which a strong ASOC is expected from their large atomic numbers, demonstrate conventional *s*-wave superconductivity. On the other hand, two-gap superconductivity has been shown in Y_2C_3 ,¹⁹ La_2C_3 ,²⁰ $\text{Mg}_{10}\text{Ir}_{19}\text{B}_{16}$,²¹ BiPd ^{50,51} and LaNiC_2 (this work). In Y_2C_3 , evidence of line nodes was noticed in the low temperature limit, even though the ASOC is weak in this compound.¹⁹ According to the available experiments, we are, besides $\text{Li}_2\text{Pt}_3\text{B}$, still short of examples showing spin-triplet superconductivity in NCS compounds with weak electron correlations. The ASOC can enhance the upper critical field which can nicely explain the extremely large value of $B_{c2}(0)$ and its anisotropy in the heavy fermion NCS SCs.^{12,13,55} However, in the weakly correlated NCS SCs like $\text{Li}_2\text{Pt}_3\text{B}$ ⁴¹ and BaPtSi_3 ,⁵² $B_{c2}(0)$ is rather small even though the ASOC is strong in these compounds. Moreover, the upper critical field $B_{c2}(T)$ of $\text{Li}_2(\text{Pd}_{1-x}\text{Pt}_x)_3\text{B}$ behaves similarly at different doping concentrations and can be scaled by the corresponding T_c .⁴¹ In contrast, a large upper critical field $B_{c2}(0)$ is observed in Y_2C_3 ,¹⁹ La_2C_3 ²⁰ and $\text{Mo}_3\text{Al}_2\text{C}$,⁵⁶ of which the ASOC strength is relatively weak. All these experimental facts seem to indicate that the ASOC effect may not be the sole determining parameter of the superconducting properties in NCS SCs. A systematic study, both experimental and theoretical, remains highly desired in order to elucidate the nature of superconductivity in NCS compounds.

IV. CONCLUSION

In summary, we have systematically measured the low temperature London penetration depth, specific heat and electrical resistivity in order to probe the superconducting order parameter in the weakly correlated, non-centrosymmetric su-

TABLE I: Superconducting parameters in some major non-centrosymmetric superconductors. Since the ASOC strength is expected to be proportional to the square of the atomic numbers for atoms on the NCS crystalline sites, we assign the band splitting E_{ASOC} with "large" or "small" by their atomic numbers in case that no band structure calculations are available.

Material	Space Group	T_c [K]	$B_{c2}(0)$ [T]	γ_n [mJ/mol·K ²]	E_{ASOC}	Pairing State	Ref.
CePt ₃ Si	Tetragonal $P4mm$	0.75(max)	3.2($H \parallel c$), 2.7($H \perp c$)	390	200meV	singlet & triplet	6,8–10
CeIrSi ₃	Tetragonal $I4mm$	1.6(max)	45($H \parallel c$), 11($H \perp c$)	100	4meV	triplet	13,45,46
CeRhSi ₃	Tetragonal $I4mm$	1.05(max)	30($H \parallel c$), 7($H \perp c$)	110	10meV	triplet	12,47
Li ₂ Pt ₃ B	Cubic $P4_32$	2.6	1.9	7	200meV	triplet	15–18
Li ₂ Pd ₃ B	Cubic $P4_32$	7.6	6.2	9	30meV	<i>s</i> -wave	15–18
LaNiC ₂	Orthogonal $Amm2$	2.75	1.67	7.7	42meV	two-gap	this work, ⁴⁴
Y ₂ C ₃	Cubic $I\bar{4}3d$	16	29	6.3	15meV	two-gap	19,48
La ₂ C ₃	Cubic $I\bar{4}3d$	13.2	19	10.6	30meV	two-gap	20,49
Mg ₁₀ Ir ₁₉ B ₁₆	Cubic $I\bar{4}3m$	5	0.77	52.6	<i>large</i>	two-gap	21
BiPd	Monoclinic $P2_1$	3.8	0.8($H \parallel b$)	4	<i>large</i>	two-gap	50,51
BaPtSi ₃	Tetragonal $I4mm$	2.25	0.05	5.7	<i>large</i>	<i>s</i> -wave	52
Re ₃ W	Cubic $I\bar{4}3m$	7.8	12.5	15.9	<i>large</i>	<i>s</i> -wave	53
Ir ₂ Ga ₉	Monoclinic Pc	2.25	0.025	6.9	<i>large</i>	<i>s</i> -wave	54
Rh ₂ Ga ₉	Monoclinic Pc	1.95	type-I	7.9	<i>small</i>	<i>s</i> -wave	54
Mo ₃ Al ₂ C	Cubic $P4_132$	9	15.7	17.8	<i>small</i>	<i>s</i> -wave	56,57
Ru ₇ B ₃	Hexagonal $P6_3mc$	3.3	1.7($H \parallel c$), 1.6($H \perp c$)	43.7	<i>small</i>	<i>s</i> -wave	58

perconductor LaNiC₂. It was found that both the penetration depth $\Delta\lambda(T)$ and the electronic specific heat $C_e(T)$ show exponential-like behavior at low temperatures which can be fitted by a two-gap BCS model. The upper critical field $B_{c2}(T)$ is enhanced at low temperatures, as a result of the contributions from the small superconducting gap. The residual Sommerfeld coefficient, $\gamma_0(B)$, increases rapidly at low fields, and eventually gets saturated with further increasing magnetic field. All these experimental facts provide unambiguous evidence for two-gap superconductivity for LaNiC₂. We argue that such a superconducting state may arise from the moderate ASOC strength in LaNiC₂, which leads to a moderate band splitting E_{ASOC} and a mixed pairing state with comparable spin-singlet and spin-triplet pairing components.

V. ACKNOWLEDGEMENTS

We acknowledge valuable discussion with M. Sigrist, E. Bauer and M. B. Salamon. This work was supported by the Natural Science Foundation of China (Grant No. 10934005), the National Basic Research Program of China (Grant Nos. 2009CB929104, 2011CBA00103), Zhejiang Provincial Natural Science Foundation of China, the Fundamental Research Funds for the Central Universities, and the Max-Planck Society under the auspices of the Max-Planck partner group of the MPI for Chemical Physics of Solids, Dresden.

- * Electronic address: hqyuan@zju.edu.cn
- ¹ P. W. Anderson, J. Phys. Chem. Solids **11**, 26 (1959).
 - ² P. W. Anderson, Phys. Rev. B **30**, 4000 (1984).
 - ³ L. P. Gor'kov and E. I. Rashba, Phys. Rev. Lett. **87**, 037004 (2001).
 - ⁴ S. K. Yip, Phys. Rev. B **65**, 144508 (2002).
 - ⁵ P. A. Frigeri, D. F. Agterberg, A. Koga, and M. Sigrist, Phys. Rev. Lett. **92**, 097001 (2004).
 - ⁶ K. V. Samokhin, E. S. Zijlstra, and S. K. Bose, Phys. Rev. B **69**, 094514 (2004); **70**, 069902(E) (2004).
 - ⁷ S. Fujimoto, J. Phys. Soc. Jpn. **76**, 051008 (2007).
 - ⁸ E. Bauer, G. Hilscher, H. Michor, Ch. Paul, E. W. Scheidt, A. Gribanov, Yu. Seropegin, H. Noël, M. Sigrist, and P. Rogl, Phys. Rev. Lett. **92**, 027003 (2004).
 - ⁹ M. Yogi, Y. Kitaoka, S. Hashimoto, T. Yasuda, R. Settai, T. D. Matsuda, Y. Haga, Y. Ōnuki, P. Rogl, and E. Bauer, Phys. Rev. Lett. **93**, 027003 (2004).
 - ¹⁰ I. Bonalde, W. Brämer-Escamilla, and E. Bauer, Phys. Rev. Lett. **94**, 207002 (2005).
 - ¹¹ M. Nicklas, F. Steglich, J. Knolle, I. Eremin, R. Lackner, and E. Bauer, Phys. Rev. B **81**, 180511(R) (2010).
 - ¹² N. Kimura, K. Ito, H. Aoki, S. Uji, and T. Terashima, Phys. Rev. Lett. **98**, 197001 (2007).
 - ¹³ R. Settai, Y. Miyauchi, T. Takeuchi, F. Lvy, I. Sheikin, and Y. Ōnuki, J. Phys. Soc. Jpn. **77**, 073705 (2008).
 - ¹⁴ T. Akazawa, H. Hidaka, H. Kotegawa, T. C. Kobayashi, T. Fujiwara, E. Yamamoto, Y. Haga, R. Settai, and Y. Ōnuki, J. Phys. Soc. Jpn. **73**, 3129 (2004).
 - ¹⁵ H. Q. Yuan, D. F. Agterberg, N. Hayashi, P. Badica, D. Vandervelde, K. Togano, M. Sigrist, and M. B. Salamon, Phys. Rev. Lett. **97**, 017006 (2006). H. Q. Yuan, M. B. Salamon, P. Badica, and K. Togano, Physica B **403**, 1138 (2008).
 - ¹⁶ M. Nishiyama, Y. Inada, and G. Q. Zheng, Phys. Rev. Lett. **98**, 047002 (2007).
 - ¹⁷ H. Takeya, M. ElMassalami, S. Kasahara, and K. Hirata, Phys. Rev. B **76**, 104506 (2007).
 - ¹⁸ K. W. Lee and W. E. Pickett, Phys. Rev. B **72**, 174505 (2005).
 - ¹⁹ J. Chen, M. B. Salamon, S. Akutagawa, J. Akimitsu, J. Singleton, J. L. Zhang, L. Jiao, and H. Q. Yuan, Phys. Rev. B **83**, 144529 (2011).

- ²⁰ S. Kuroiwa, Y. Saura, J. Akimitsu, M. Hiyaishi, M. Miyazaki, K. H. Satoh, S. Takeshita, and R. Kadono, *Phys. Rev. Lett.* **100**, 097002 (2008).
- ²¹ T. Klimczuk, F. Ronning, V. Sidorov, R. J. Cava, and J. D. Thompson, *Phys. Rev. Lett.* **99**, 257004 (2007).
- ²² O. I. Bodak and E. P. Marusin, *Dopov. Akad. Nauk Ukr. RSR A* **12**, 1048 (1979).
- ²³ V. K. Pecharsky, L. L. Miller, and K. A. Gschneidner, *Phys. Rev. B* **58**, 497 (1998).
- ²⁴ Y. Iwamoto, Y. Iwasaki, K. Ueda, and T. Kohara, *Phys. Lett. A* **250**, 439 (1998).
- ²⁵ A. Subedi and D. J. Singh, *Phys. Rev. B* **80**, 092506 (2009).
- ²⁶ I. Bonalde, R. L. Ribeiro, K. J. Syu, H. H. Sung, and W. H. Lee, *New J. Phys.* **13**, 123022 (2011).
- ²⁷ W. H. Lee, H. K. Zeng, Y. D. Yao, Y. Y. Chen, *Physica C* **266**, 138 (1996).
- ²⁸ A. D. Hillier, J. Quintanilla, and R. Cywinski, *Phys. Rev. Lett.* **102**, 117007 (2009).
- ²⁹ J. Quintanilla, A. D. Hillier, J. F. Annett, and R. Cywinski, *Phys. Rev. B* **82**, 174511 (2010).
- ³⁰ A. Carrington and F. Manzano, *Physica C* **385**, 205 (2003).
- ³¹ F. Bouquet, Y. Wang, R. A. Fisher, D. G. Hinks, J. D. Jorgensen, A. Junod, and N. E. Phillips, *Europhys. Lett.* **56**, 856 (2001).
- ³² F. Bouquet, R. A. Fisher, N. E. Phillips, D. G. Hinks, and J. D. Jorgensen, *Phys. Rev. Lett.* **87**, 047001 (2001).
- ³³ K. H. Müller, G. Fuchs, A. Handstein, K. Nenkov, V. N. Narozhnyi, and D. Eckert, *J. Alloys Comp.* **322**, L10 (2001).
- ³⁴ B. D. Yanoff, Ph.D. thesis, University of Illinois at Urbana-Champaign, 2000.
- ³⁵ F. Gross, B. S. Chandrasekhar, D. Einzel, K. Andres, P. J. Hirschfeld, H. R. Ott, J. Beuers, Z. Fisk, and J. L. Smith, *Z. Phys. B: Condens. Matt.* **64**, 175 (1986).
- ³⁶ T. Park, H. Lee, I. Martin, X. Lu, V. A. Sidorov, K. Gofryk, F. Ronning, E. D. Bauer, and J. D. Thompson, *Phys. Rev. Lett.* **108**, 077003 (2012).
- ³⁷ A. Mirmelstein, A. Junod, E. Walker, B. Revaz, J. Y. Genoud, and G. Triscone, *J. Supercond.* **10**, 527 (1997).
- ³⁸ C. Caroli, P. G. de Gennes, and J. Matricon, *Phys. Rev. Lett.* **9**, 307 (1964).
- ³⁹ G. E. Volovik, *JETP Lett.* **58** 469 (1993).
- ⁴⁰ R. W. Hill, S. Y. Li, M. B. Maple, and L. Taillefer, *Phys. Rev. Lett.* **101**, 237005 (2008).
- ⁴¹ D. C. Peet, G. Eguchi, M. Kriener, S. Harada, Sk. Md. Shamsuz-zamen, Y. Inada, G. Q. Zheng, and Y. Maeno, *Phys. Rev. B* **84**, 054521 (2011).
- ⁴² N. R. Werthamer, E. Helfand, and P. C. Hohenberg, *Phys. Rev.* **147**, 295 (1966).
- ⁴³ A. Gurevich, *Phys. Rev. B* **67**, 184515 (2003).
- ⁴⁴ I. Hase and T. Yanagisawa, *J. Phys. Soc. Jpn.* **78**, 084724 (2009).
- ⁴⁵ H. Mukuda, T. Ohara, M. Yashima, Y. Kitaoka, R. Settai, Y. Ōnuki, K. M. Itoh, and E. E. Haller, *Phys. Rev. Lett.* **104**, 017002 (2010).
- ⁴⁶ T. Kawai, H. Muranaka, T. Endo, N. D. Dung, Y. Doi, S. Ikeda, T. D. Matsuda, Y. Haga, H. Harima, R. Settai, and Y. Ōnuki, *J. Phys. Soc. Jpn.* **77**, 064717 (2008).
- ⁴⁷ T. Terashima, M. Kimata, S. Uji, T. Sugawara, N. Kimura, H. Aoki, and H. Harima, *Phys. Rev. B* **78**, 205107 (2008).
- ⁴⁸ Y. Nishikayama, T. Shishidou, and T. Oguchi, *J. Phys. Soc. Jpn.* **76**, 064714 (2007).
- ⁴⁹ S. Kim, W. Xie, R. K. Kremer, V. Babizhetskyy, O. Jepsen, A. Simon, K. S. Ahm, B. Raquet, H. Rakoto, J. M. Broto, and B. Ouladdiaf, *Phys. Rev. B* **76**, 014516 (2007).
- ⁵⁰ B. Joshi, A. Thamizhavel, and S. Ramakrishnan, *Phys. Rev. B* **84**, 064518 (2011).
- ⁵¹ M. Mondal, B. Joshi, S. Kumar, A. Kamlapure, S. C. Ganguli, A. Thamizhavel, S. S. Mandal, S. Ramakrishnan, and P. Raychaudhuri, e-print arXiv:1202.2454.
- ⁵² E. Bauer, R. T. Khan, H. Michor, E. Royanian, A. Grytsiv, N. Melnychenko-Koblyuk, P. Rogl, D. Reith, R. Podloucky, E. W. Scheidt, W. Wolf, and M. Marsman, *Phys. Rev. B* **80**, 064504 (2009).
- ⁵³ Y. L. Zuev, V. A. Kuznetsova, R. Prozorov, M. D. Vannette, M. V. Lobanov, D. K. Christen, and J. R. Thompson, *Phys. Rev. B* **76**, 132508 (2007).
- ⁵⁴ K. Wakui, S. Akutagawa, N. Kase, K. Kawashima, T. Muranaka, Y. Iwahori, J. ABE, and J. Akimitsu, *J. Phys. Soc. Jpn.* **78**, 034710 (2009).
- ⁵⁵ R. P. Kaur, D. F. Agterberg, and M. Sgrist, *Phys. Rev. Lett.* **94**, 137002 (2005).
- ⁵⁶ E. Bauer, G. Rogl, X. Q. Chen, R. T. Khan, H. Michor, G. Hilscher, E. Royanian, K. Kumagai, D. Z. Li, Y. Y. Li, R. Podloucky, and P. Rogl, *Phys. Rev. B* **82**, 064511 (2010).
- ⁵⁷ I. Bonalde, H. Kim, R. Prozorov, C. Rojas, P. Rogl, and E. Bauer, *Phys. Rev. B* **84**, 134506 (2011).
- ⁵⁸ N. Kase and J. Akimitsu, *J. Phys. Soc. Jpn.* **78**, 044710 (2009).